

# Total density profile of massive early-type galaxies in Horizon-AGN simulation: impact of AGN feedback and comparison with observations

Sébastien Peirani<sup>1,2,3,4\*</sup>, Alessandro Sonnenfeld<sup>3</sup>, Raphaël Gavazzi<sup>2</sup>,  
Masamune Oguri<sup>3,4,5</sup>, Yohan Dubois<sup>2</sup>, Joe Silk<sup>2,6,8</sup>, Christophe Pichon<sup>2,9</sup>,  
Julien Devriendt<sup>6,7</sup> and Sugata Kaviraj<sup>10</sup>

<sup>1</sup> *Université Côte d’Azur, Observatoire de la Côte d’Azur, CNRS, Laboratoire Lagrange, Bd de l’Observatoire, CS 34229, 06304 Nice Cedex 4, France*

<sup>2</sup> *Institut d’Astrophysique de Paris (UMR 7095: CNRS & UPMC), 98 bis Bd Arago, 75014 Paris, France*

<sup>3</sup> *Kavli IPMU (WPI), UTIAS, The University of Tokyo, Kashiwa, Chiba 277-8583, Japan*

<sup>4</sup> *Department of Physics, The University of Tokyo, 7-3-1 Hongo, Bunkyo-ku, Tokyo 113-0033, Japan*

<sup>5</sup> *Research Center for the Early Universe, School of Science, The University of Tokyo, 7-3-1 Hongo, Bunkyo-ku, Tokyo 113-0033, Japan*

<sup>6</sup> *Sub-department of Astrophysics, University of Oxford, Keble Road, Oxford OX1 3RH*

<sup>7</sup> *Observatoire de Lyon, UMR 5574, 9 avenue Charles André, Saint Genis Laval 69561, France*

<sup>8</sup> *Department of Physics and Astronomy, The Johns Hopkins University Homewood Campus, Baltimore, MD 21218, USA*

<sup>9</sup> *Korea Institute of Advanced Studies (KIAS) 85 Hoegiro, Dongdaemun-gu, Seoul, 02455, Republic of Korea*

<sup>10</sup> *Centre for Astrophysics Research, University of Hertfordshire, College Lane, Hatfield, Herts, AL10 9AB, UK*

19 December 2018

## ABSTRACT

Using the two large cosmological hydrodynamical simulations, HORIZON-AGN ( $H_{\text{AGN}}$ ) and HORIZON-NOAGN ( $H_{\text{noAGN}}$ , no AGN feedback), we investigate how a typical sub-grid model for AGN feedback affects the evolution of the total density profiles (dark matter + stars) at the effective radius of massive early-type galaxies ( $M_* \geq 10^{11} M_\odot$ ). We have studied the dependencies of the mass-weighted density slope  $\gamma'_{\text{tot}}$  with the effective radius, the galaxy mass and the host halo mass at  $z \sim 0.3$  and found that the inclusion of AGN feedback always leads to a much better agreement with observational values and trends. Our analysis suggests also that the inclusion of AGN feedback favours a strong correlation between  $\gamma'_{\text{tot}}$  and the density slope of the dark matter component while, in the absence of AGN activity,  $\gamma'_{\text{tot}}$  is rather strongly correlated with the density slope of the stellar component. Finally, we find that  $\gamma'_{\text{tot}}$  derived from our samples of galaxies increases from  $z = 2$  to  $z = 0$ , in good agreement with the expected observational trend. The derived slopes are slightly lower than in the data when AGN is included because the simulated galaxies tend to be too extended, especially the least massive ones. However, the simulated compact galaxies without AGN feedback have  $\gamma'_{\text{tot}}$  values that are significantly too high compared to observations.

**Key words:** Galaxies: evolution – Galaxies: jets – Galaxies: haloes – Dark matter – Methods: numerical

## 1 INTRODUCTION

Despite the early discovery of tight scaling relations between the physical properties of the apparently simple “red and dead” population of

\* E-mail: sebastien.peirani@oca.eu

early-type galaxies (ETGs), the origin and evolution of these relations are still poorly understood (White & Rees 1978; Dressler et al. 1987; Faber et al. 1987; Djorgovski & Davis 1987). These properties concern the stellar mass profile, stellar populations, metallicity, halo mass to stellar mass relation, as well as stellar mass to central supermassive black hole mass (Magorrian et al. 1998; Ferrarese & Merritt 2000; Häring & Rix 2004; Gültekin et al. 2009). In the standard  $\Lambda$ CDM paradigm, progenitors of massive collapsed structures such as massive ETGs form at high redshift by the accretion of cold filamentary gas (Rees & Ostriker 1977; White & Frenk 1991; Birnboim & Dekel 2003; Kereš et al. 2005; Ocvirk et al. 2008; Dekel et al. 2009; van de Voort et al. 2011) that must be stopped at low redshift by some feedback mechanism associated with the central Active Galactic Nucleus (AGN) (Silk & Rees 1998; King 2003; Wyithe & Loeb 2003). The emerging picture is that they are formed at a redshift larger than 3 and almost fully assembled by  $z \sim 1$  (e.g. Renzini 2006). One important conclusion is that their central regions must be virialized with a self-similar structure as early as  $z \sim 1$  (Sheth et al. 2003) irrespective of the continuous accretion of dark and luminous matter within the  $\Lambda$ CDM hierarchical merging process. This ETG property may be explained if internal regions (within  $\sim 2$  effective radii) behave like a dynamical attractor featuring an invariant phase space density in spite of their accretion history (Loeb & Peebles 2003). The dark matter and stellar components seem to work together in building a “universal” nearly isothermal total density profile, even though neither of these components is well approximated by an isothermal profile.

In the past few years, the deep study of early-type galaxies playing the role of strong gravitational lenses has led to major developments in the observational side. Indeed, the strong lensing allows very accurate estimation of the total mass at the Einstein radius of such systems and can therefore be combined with other traditional methods such as stellar velocity dispersion (Miralda-Escude 1995; Natarajan & Kneib 1996; Treu & Koopmans 2002; Sand et al. 2002; Newman et al. 2009), and stellar mass maps from multicolor imaging and/or spectroscopy. Such a combination is expected to break the degeneracies inherent to each method alone such as, for instance, the mass-anisotropy degeneracy, bulge-halo degeneracy and the stellar mass/initial mass function (IMF) degeneracy (e.g. Koopmans & Treu 2003; Treu & Koopmans 2004; Treu et al. 2010; Auger et al. 2010; Dutton et al. 2013). Weak lensing analysis can also provide additional constraints though it is not yet possible to use for individual galaxies (Gavazzi et al. 2007; Jiang & Kochanek 2007; Lagattuta et al. 2010). Another way to break the degeneracy in the analysis of strong lens systems is to use quasar microlensing which directly measures the stellar mass function at the image position (e.g. Oguri et al. 2014; Schechter et al. 2014; Jiménez-Vicente et al. 2015).

The sample assembled by the SLACS team has shown that lensing galaxies are indistinguishable from

non-lensing early-type galaxies with similar velocity dispersions in terms of their internal properties and environment (Bolton et al. 2006; Koopmans et al. 2006; Treu et al. 2006; Gavazzi et al. 2007; Bolton et al. 2008; Treu et al. 2009; Koopmans et al. 2009; Auger et al. 2009, 2010; Barnabè et al. 2011; Czoske et al. 2012; Shu et al. 2015). Additional samples of higher redshift lenses with measured velocity dispersion have then been built, such as the Strong Lensing Legacy Survey (Tu et al. 2009; Gavazzi et al. 2014; Ruff et al. 2011a; Sonnenfeld et al. 2013a; Gavazzi et al. 2012; Sonnenfeld et al. 2013b, 2015) or BOSS Emission-line Lens Survey (Brownstein et al. 2012; Bolton et al. 2012; Shu et al. 2016) and allowed one to investigate the time dependence of the slope of the inner total mass density profile near the effective radius (see also Tortora et al. 2014; Dye et al. 2014; Posacki et al. 2015; Smith et al. 2015). At fixed mass, the total density slope correlates with the projected stellar mass density and seems to decrease with redshift while remaining close to isothermal ( $\gamma' \equiv -d \log \rho / d \log r \simeq 2$ , with a noticeably small  $\sim 6\%$  intrinsic scatter). Similar conclusions can be drawn from spatially resolved stellar kinematics of ETGs (see e.g. Cappellari 2016, for a review). In addition, the combination of strong lensing and stellar kinematics at group and cluster scales can also provide us with sizable statistical samples (Newman et al. 2013, 2015) for extending our understanding of galaxy formation towards the high mass end.

In parallel to these observational efforts, several attempts were made to understand the origin and the tightness of this relation, either with semi-analytical models or idealized simulations (Nipoti et al. 2009; Lackner & Ostriker 2010; Nipoti et al. 2012; Lackner et al. 2012; Hirschmann et al. 2012; Johansson et al. 2012; Remus et al. 2013; Dutton & Treu 2014; Sonnenfeld et al. 2014; Shankar et al. 2017). The complex coupling of scales (from dark matter haloes and beyond to star formation and AGN activity) involved for understanding this dynamical interplay between baryons and dark matter haloes requires very demanding numerical hydrodynamical simulations. An important step forward was made possible by zoomed hydrodynamical simulations around massive galaxies that contain realistic accretion scenarios and sufficient resolution to recover with good fidelity the internal structure of massive ETGs (Dubois et al. 2013). In particular, a detailed census on the role of the feedback from the central AGN was made, showing that the quenching of star formation by the central engine is not only important for reproducing stellar to halo mass relations and colors but also for reproducing the size and the dynamical structure (pressure support instead of rotation). The small statistics permitted with these zooms has recently been alleviated by a hydrodynamical simulation with RAMSES (Teyssier 2002) of larger cosmological volumes containing  $\sim 10^5$  objects with similar resolution. This was one of the purposes of the HORIZON-AGN simulation (Dubois et al. 2014, 2016; Welker et al. 2017; Kaviraj et al. 2017; Beckmann et al. 2017), who confirmed with better statistics some of the results of Dubois et al. (2013).

Recently, a comparison of the internal structure of massive ETGs in the Illustris Simulation (Vogelsberger et al. 2014) which is quite comparable to HORIZON-AGN showed reasonable agreement with observations, although the size of galaxies seems to be slightly overshoot (Xu et al. 2017). This confirms the interest in performing detailed comparisons between simulations and observations with different simulation codes and solvers in order to study degeneracies between subgrid physical recipes and solver specificities that could match observations for very different physical reasons. Hence, since we already studied in detail the role of AGN feedback on the evolution of internal dark matter and stellar density profiles from our set of HORIZON-AGN simulations (Peirani et al. 2017), we will now attempt to compare our results with the SLACS+SL2S lensing observational constraints on the internal structure of massive galaxies coming from strong lensing and dynamics, the main focus being the total mass density profile within the effective radius.

The paper is organised as follows. Section 2 briefly the numerical modelling used in this work (simulations and post-processing) while Section 3 presents our main results relative to the evolution of the total density profiles in massive ETGs. We finally conclude in Section 4.

## 2 NUMERICAL MODELLING

In this paper, we analyse and compare galaxy samples extracted from two large cosmological hydrodynamical simulations, HORIZON-AGN ( $H_{\text{AGN}}$ ) and HORIZON-NOAGN ( $H_{\text{noAGN}}$ ). These simulations and galaxies/dark matter haloes samples production have been already described in great details in Dubois et al. (2014, 2016) and Peirani et al. (2017). In the following, we only summarise the main features.

### 2.1 Horizon-AGN and Horizon-noAGN

The HORIZON-AGN simulation (Dubois et al. 2014) considers a standard  $\Lambda$ CDM cosmology with total matter density  $\Omega_m = 0.272$ , dark energy density  $\Omega_\Lambda = 0.728$ , amplitude of the matter power spectrum  $\sigma_8 = 0.81$ , baryon density  $\Omega_b = 0.045$ , Hubble constant  $H_0 = 70.4 \text{ km s}^{-1} \text{ Mpc}^{-1}$ , and  $n_s = 0.967$  compatible with the WMAP-7 (Komatsu et al. 2011). The simulation was performed in a periodic box of side  $L_{\text{box}} = 100 h^{-1} \text{ Mpc}$  containing  $1024^3$  dark matter (DM) particles, resulting in a DM mass resolution of  $M_{\text{DM, res}} = 8.27 \times 10^7 M_\odot$ . The simulation is run with the RAMSES code (Teyssier 2002), and the initially uniform grid is adaptively refined down to  $\Delta x = 1$  proper kpc at all times.

HORIZON-AGN includes gas dynamics, gas cooling and heating (from an uniform UV background taking place after redshift  $z_{\text{reion}} = 10$ ), and various sub-grid models such as: star formation, feedback from stars (stellar winds, type Ia and type II supernovae), metal enrichment of the interstellar medium by following six chemical species (O, Fe, C, N, Mg, Si). Black hole (BH) formation and growth are also included. We consider a

Bondi-Hoyle-Lyttleton accretion rate on to BHs namely  $\dot{M}_{\text{BH}} = 4\pi\alpha G^2 M_{\text{BH}}^2 \bar{\rho} / (\bar{c}_s^2 + \bar{u}^2)^{3/2}$ , where  $M_{\text{BH}}$  is the BH mass,  $\rho$  the mean gas density,  $\bar{c}_s$  the average sound speed,  $\bar{u}$  the average gas velocity relative to the BH velocity and  $\alpha$  a dimensionless boost factor defined by  $\alpha = (\rho/\rho_0)^2$  when  $\rho > \rho_0$  and  $\alpha = 1$  otherwise (Booth & Schaye 2009). The effective accretion rate on to BHs is capped at the Eddington accretion rate:  $\dot{M}_{\text{Edd}} = 4\pi G M_{\text{BH}} m_p / (\epsilon_r \sigma_T c)$  in which  $c$  is the speed of light,  $m_p$  the proton mass,  $\sigma_T$  the Thompson cross-section and  $\epsilon_r$  the radiative efficiency. In our modelling, we assumed  $\epsilon_r = 0.1$  for the Shakura & Sunyaev (1973) accretion on to a Schwarzschild BH. BHs release energy in two distinct modes: quasar (heating) or radio (kinetic jet) mode when the accretion rate  $\chi \equiv \dot{M}_{\text{BH}}/\dot{M}_{\text{Edd}}$  is  $\chi > 0.01$  and  $\chi < 0.01$  respectively. The quasar mode is modelled as an isotropic injection of thermal energy into the gas within a sphere of radius  $\Delta x$  and at an energy deposition rate  $\dot{E}_{\text{AGN}} = \epsilon_f \epsilon_r \dot{M}_{\text{BH}} c^2$ , where  $\epsilon_f = 0.15$  is a free parameter used to match the BH-galaxy scaling relations (see Dubois et al. (2012) for detail). At low accretion rates, energy is released through AGN radio mode into a bipolar outflow with a jet velocity of  $10^4 \text{ km s}^{-1}$ . Following Omma et al. (2004), a cylinder with a cross-sectional radius  $\Delta x$  and height  $2\Delta x$  is used to model the outflow (see Dubois et al. (2010) for details). In this case, the efficiency of the radio mode is larger than the quasar mode with  $\epsilon_f = 1$ . In Fig. 5 of Peirani et al. (2017), we have studied the evolution of the Eddington ratio  $\chi$  over relevant dark matter halo mass ranges. Our results strongly indicate that the radio mode tends to be the dominant mode below  $z \lesssim 2$ . These results are also in agreement with Volonteri et al. (2016) who have studied in detail the cosmic evolution of black holes in the HORIZON-AGN simulation.

HORIZON-NOAGN was performed using the same set of initial conditions and sub-grid modelling but with no black hole formation and therefore no AGN feedback. The stellar feedback has not been changed between the two simulations, and we insist on the fact that the stellar feedback in Horizon-AGN is not “tuned” to match any galaxy properties. In both simulations, the stellar mass resolution is  $M_{*, \text{res}} = 2 \times 10^6 M_\odot$ .

Finally, it is worth mentioning that the HORIZON-AGN simulation has been extensively analysed in order to make theoretical predictions to be compared to observational data. In particular, the statistical properties of the simulated galaxies has been studied, showing good agreement with observed stellar mass functions all the way to  $z \sim 6$  (Kaviraj et al. 2017). The colour and star formation histories are also well recovered as well as the so called black hole - bulge relations and duty-cycles of AGNs (Volonteri et al. 2016).

### 2.2 Galaxy catalogues

Galaxies are identified using the ADAPTAHOP (sub)halo finder (Aubert et al. 2004) and for the present study, we mainly focus on galaxies with a mass greater than  $10^{11} M_\odot$ . We use also the most bound particle as the definition of their centre. For each given  $H_{\text{AGN}}$  or  $H_{\text{noAGN}}$

galaxy, we compute the radial, tangential and vertical velocity components of each stellar particle where the orientation of the z-axis cylindrical coordinate is defined by the spin vector (i.e. the angular momentum vector from the stellar component). Then, we estimate the rotational velocity  $V$  of the galaxy by computing the average of the tangential velocity component. The velocity dispersion  $\sigma$  is obtained from the dispersion of the radial  $\sigma_r$ , the tangential  $\sigma_\theta$  and the vertical velocity  $\sigma_z$  components around their averaged values namely  $\sigma^2 = (\sigma_r^2 + \sigma_\theta^2 + \sigma_z^2)/3$ . In our analysis, we select in general  $H_{\text{AGN}}$  and  $H_{\text{noAGN}}$  galaxies with  $V/\sigma < 1$  because we are interested in ETGs only.

Finally, in order to match galaxies between  $H_{\text{AGN}}$  and  $H_{\text{noAGN}}$  simulations, we use the scheme developed in Peirani et al. (2017). To summarize, we first match host dark matter haloes between the two simulations. To do so, we use the fact that, as we start from the same initial conditions, each dark matter particle possesses an identity which is identical among the twin simulations. Then, if more than 75% of the particles of any given halo in the HORIZON-AGN can also be found in a halo identified in the HORIZON-NOAGN, we conclude that these haloes are associated (provided that their mass ratio is lower than 10 or greater than 0.1). This scheme cannot be repeated to match galaxies since stellar particles are created during the simulations and do not necessarily correspond between the two runs. Therefore, we first couple each galaxy to a host dark matter halo in their parent simulation by choosing the most massive galaxy whose centre is located within a sphere of radius equal to 5% of the virial radius of its host halo. Galaxy pairs between the two simulation are then determined through the matching of their host halo as previously described. Note that past numerical works suggest that the presence of AGN feedback allows mergers to durably transform rotationally-supported discs ( $V/\sigma > 1$ ) into dispersion-dominated ellipsoids ( $V/\sigma < 1$ ) (Dubois et al. 2013, 2016). Therefore, when using our matching algorithm,  $H_{\text{AGN}}$  galaxies satisfying  $V/\sigma < 1$  might be associated to  $H_{\text{noAGN}}$  galaxies with  $V/\sigma > 1$ .

### 3 THE TOTAL DENSITY SLOPES AT THE EFFECTIVE RADIUS

#### 3.1 Definitions

In the present study, we focus on the *mass-weighted density slope within  $r_1$  and  $r_2$*  introduced by Dutton & Treu (2014):

$$\gamma' = \frac{1}{M(r_2) - M(r_1)} \int_{r_1}^{r_2} \gamma(x) 4\pi x^2 \rho(x) dx \quad (1)$$

where  $\gamma \equiv -d \log \rho / d \log r$  is the local logarithmic slope of the density profile  $\rho$  and  $M$  the local mass. Using a discrete representation of each density profile,  $\gamma(r)$  and  $M(r)$  can be estimated within each radial bin.

For each studied galaxy, we have considered a random orientation in space and then derive the effective radius  $R_e$  at which half of the projected stellar mass

is enclosed. Finally, in order to estimate  $\gamma'$  at  $R_e$ , we consider the interval  $[r_1 - r_2] = [R_e/2 - R_e]$  since it corresponds to radii probed by the strong lens samples used in this paper. In strong lensing + dynamics studies, the total density slope  $\gamma'$  is observationally determined by fitting a power-law density profile to the Einstein radius and central velocity dispersion (Koopmans et al. 2006). Strictly speaking, the value of  $\gamma'$  recovered in this way is equal to the mass-weighted slope of the lens only if its true density profile is a power-law. Nevertheless, Sonnenfeld et al. (2013b) showed how these two definitions of the slope give values of  $\gamma'$  that are typically within 0.05 of each other, for a variety of lens density profiles (see also Xu et al. 2017, for a detailed study). Note also that the simulation grid size has a value of 1 kpc where dark matter or galaxy density profiles might not fully converge. In the Appendix A, we have performed a convergence study in the same way than Duffy et al. (2010) and found that the lower limit value of  $\sim 5$  kpc recommended by Power et al. (2003) for our studied halo/galaxy mass range, is suitable in our analysis, though their work concerns pure dark matter simulations only. In general, the effective radius of  $H_{\text{AGN}}$  galaxies is always larger than 5 kpc. However, this is not the case for  $H_{\text{noAGN}}$  galaxies and therefore, in certain cases, we will remove galaxies with too low effective radii (i.e.  $R_e/2 \leq 1 - 2$  kpc).

In the following, we will refer respectively to  $\gamma'_{dm}$ ,  $\gamma'_*$  and  $\gamma'_{tot}$  the mass-weighted density slope derived from the dark matter component, the stellar component and the dark matter + stellar components.

#### 3.2 Dependencies of $\gamma'_{tot}$ with $R_e$ , $M_{halo}$ and $M_*$

Fig. 1 shows the variations of the effective radius  $R_e$  with respect to the stellar mass  $M_*$  for  $H_{\text{AGN}}$  and  $H_{\text{noAGN}}$  galaxies with a mass greater than  $10^{11} M_\odot$  and  $V/\sigma < 1$  at  $z = 0.3$ . We chose this latter redshift value because the observational data we want to compare with, in particular SLACS, SL2S and Newman et al. (2013, 2015), are centred around this value. The observed values of the stellar mass depend upon the assumption of a stellar initial mass function (IMF). For our comparison we assume a Salpeter IMF, which is found to be consistent with stellar masses derived from the combination of lensing and dynamics in the sample of SLACS and SL2S lenses (Sonnenfeld et al. 2015). First, we see clearly that in the absence of AGN feedback, the simulated galaxies are generally clearly too compact with an effective radius too small, compared to observational data. Note however that for  $H_{\text{noAGN}}$  galaxies with  $\log(M_*/M_\odot) < 11.5$ , the theoretical predictions seems to agree well with observations. This might be due to the fact that as the effective radius get closer to the resolution limit, their value might be overestimated. On the contrary, AGN feedback tends to form more extended galaxies as already noted by Dubois et al. (2013). In this case, high-mass ellipticals in HORIZON-AGN are in good agreement with the observations while low-mass ellipticals seem to be not compact enough. This effect could be attributed again to limited spatial resolution, as the size of low-to-



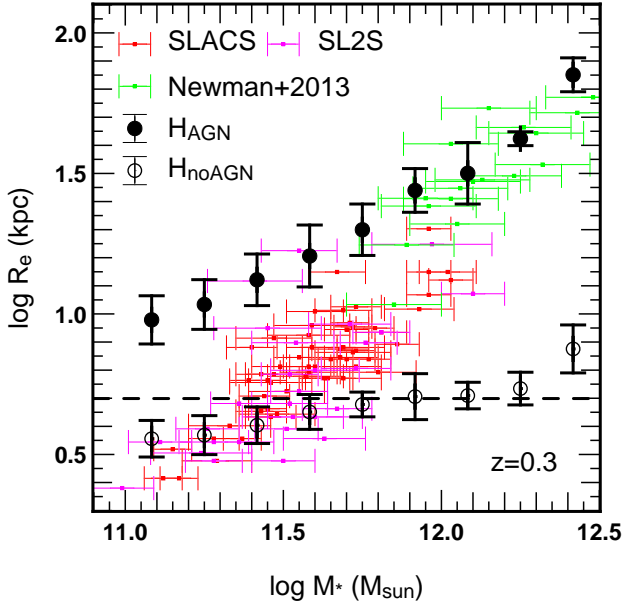


**Figure 1.** The variations of the effective radius  $R_e$  with respect to the stellar mass  $M_*$ . Results are derived from  $H_{AGN}$  (black points) and  $H_{noAGN}$  (white points) galaxies satisfying  $V/\sigma < 1$  and  $\log(M_*/M_\odot) > 11$  at  $z = 0.3$ . We also plot observational data from the SLACS, SL2S and Newman et al. (2013) which cover the redshift range of [0.063 - 0.884] but centred around  $z \sim 0.3$ . Error bars indicate the  $1\sigma$  standard deviations using a confidence interval on the scatter in a bin. For indicative purposes only, the horizontal dashed lines at  $R_e = 5$  kpc indicates a recommended resolution limit following Power et al. (2003).

intermediate mass galaxies is only a few times the spatial resolution, and can get some spurious dynamical support. Therefore, galaxy sizes are supposed to converge to  $\sim \Delta x = 1$  kpc at the low-mass end, and it is well plausible that the low-mass galaxies will get more compact with increased spatial resolution. Also, it is worth mentioning that the lensing probability  $p$  is a steep function of the velocity dispersion of galaxies  $\sigma$  (i.e.  $p \approx \sigma^4$ ). Then, for a given stellar mass, more compact galaxies will be selected by using survey which can partly explain the discrepancies between theoretical predictions and observations here. In the following, in order to take into account this selection effect, estimations of the mean value of  $\gamma'_{tot}$  are weighted by  $\sigma^4$ . However, no significant difference is noticed in the results and conclusions when  $\gamma'_{tot}$  values are derived without this weighting.

Fig. 2 shows now the variations of the mass-weighted total density slope  $\gamma'_{tot}$  with respect to the effective radius  $R_e$  at  $z = 0.3$  for  $H_{AGN}$  and  $H_{noAGN}$  galaxies with a mass greater than  $10^{11} M_\odot$  and  $V/\sigma < 1$ . When comparing our results to observations, we get a much better agreement when AGN feedback is taken into account. Indeed, we found that  $\gamma'_{tot}$  derived from HORIZON-AGN simulation is decreasing with  $R_e$  which is consistent with the observational trend. On the contrary, an opposite evolution is obtained when AGN are not included suggesting that more extended galaxies (or

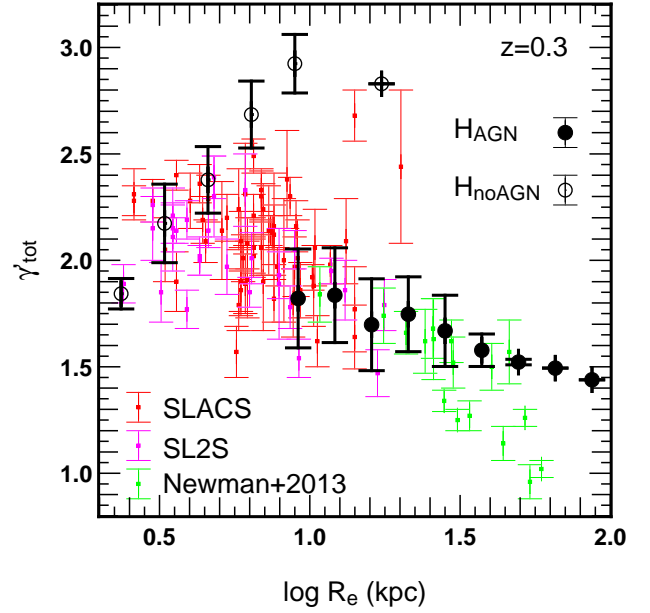


**Figure 2.** The variations of the mass-weighted total density slopes  $\gamma'_{tot}$  with respect to the effective radius  $R_e$ . Results are derived from  $H_{AGN}$  (black points) and  $H_{noAGN}$  (white points) galaxies with  $V/\sigma < 1$  and a mass of  $\log(M_*/M_\odot) > 11$  at  $z = 0.3$ . We also plot observational data from SLACS (red colors), SL2S (pink colors) and Newman et al. (2013) (green colors). Error bars indicate  $1\sigma$  standard deviations. AGN feedback is again required to improve the agreement between theoretical predictions and observational trends.

more massive galaxies) tend to have higher  $\gamma'_{tot}$  values. Moreover, for  $R_e \geq 10$  kpc, the predicted  $\gamma'_{tot}$  values derived from the HORIZON-AGN simulation are in good agreement with those of observations. In particular, we get density slopes close to 2 for the less massive galaxies of our sample which are values expected from the observations. We cannot match the observations for  $R_e < 10$  kpc since  $H_{AGN}$  low mass elliptical galaxies are too extended as shown in Fig. 1.

Our comparison between the predicted and observed mass-size relation depends also on the assumption of the stellar IMF. The data points plotted in Fig. 1 are based on a Salpeter IMF. However, a recent re-analysis of SLACS lenses shows how the presence of gradients in stellar mass-to-light ratio, required by the data, can decrease the inferred stellar masses by as much as 0.2 dex compared to the Sonnenfeld et al. (2015) values (Sonnenfeld et al. 2018). If the values of the stellar masses of SLACS lenses decrease, the data points would move in better agreement with the  $H_{AGN}$  simulation.

From the same samples of galaxies at  $z = 0.3$  (i.e.  $M_* \geq 10^{11} M_\odot$  and  $V/\sigma < 1$ ), we also take an interest in studying the variations of  $\gamma'_{tot}$  with respect to either the dark matter halo masses  $M_{halo}$  or stellar masses  $M_*$ . Those variations are displayed in Fig. 3 and 4 respectively. We find similar trends to those obtained in Fig. 2. First, the presence or not of AGN feedback leads to opposite evolution trends. When AGN feedback is included,  $\gamma'_{tot}$  is decreasing with  $M_{halo}$  or  $M_*$ . In other words, more massive objects tend to have more flat to-

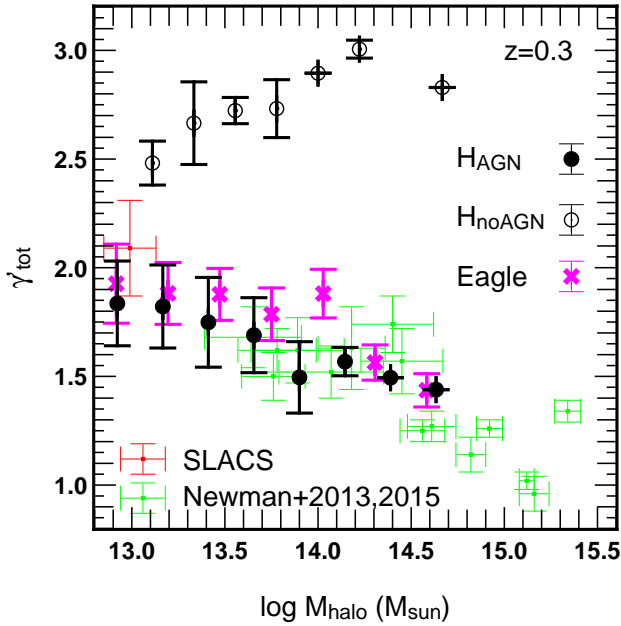


**Figure 3.** The variations of the mass-weighted total density slopes  $\gamma'_{tot}$  with respect to the dark matter halo masses  $M_{halo}$ . Results are derived from  $H_{AGN}$  (black points) and  $H_{noAGN}$  (white points) galaxies with  $V/\sigma < 1$  and a mass of  $\log(M_*/M_\odot) > 11$  at  $z = 0.3$ . We also plot observational data from SLACS (red colors) and Newman et al. (2013, 2015) (green colors) as well as predictions from the Eagle simulation. Error bars indicate  $1\sigma$  standard deviations. When AGN feedback is included, theoretical predictions are in nice agreement with observations. On the contrary, in the absence of AGN feedback, derived  $\gamma'_{tot}$  values are totally inconsistent with observational expectations.

tal density profiles at the scale of the effective radius. A similar conclusion was obtained in Peirani et al. (2017), when studying the inner DM and stellar profiles ( $r \leq 5$  kpc) which is mainly explained by the fact that AGN feedback has a more important impact in the most massive objects. Moreover, values of  $\gamma'_{tot}$  are in good agreement with observational ones. On the contrary, in the absence of AGN feedback,  $\gamma'_{tot}$  values are much too high especially for massive objects. Note that we didn't use our matching scheme here when selecting the  $H_{noAGN}$  galaxies in order to consistently compare with the observational mass range. However, we have checked that the matching scheme would select  $H_{noAGN}$  galaxies with higher masses and higher effective radius but will not really change the evolutions of  $\gamma'_{tot}$  previously derived. It is also encouraging to notice that our simulated values for  $H_{AGN}$  haloes presented in Fig. 3 are in good agreement with those of Schaller et al. (2015) using the Eagle simulation (Schaye et al. 2015). In the Appendix A, we also compare the results from lower resolution simulations. We found good agreement in the different trends relative to the variations of  $\gamma'_{tot}$  with respect to the effective radius, the dark matter halo masses and the stellar masses though there are some slight discrepancies in the variations of the effective radius with respect to the stellar masses.

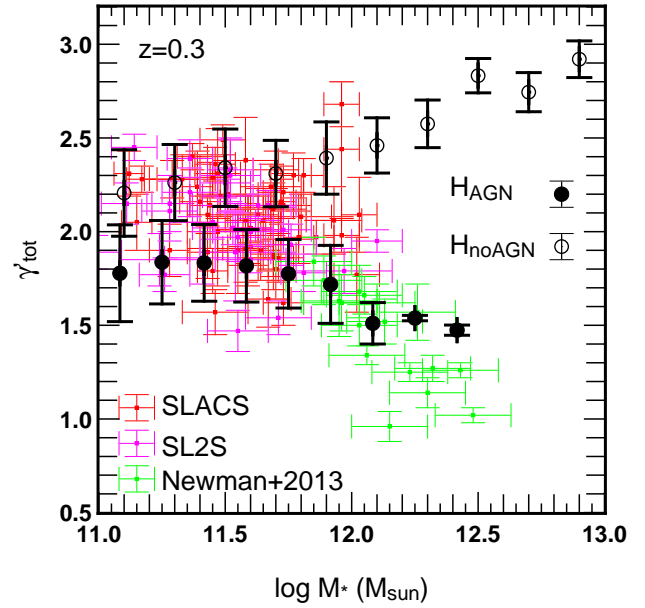


**Figure 4.** The variations of the mass-weighted total density slopes  $\gamma'_{tot}$  with respect to the stellar masses  $M_*$  at  $z = 0.3$ . Results are derived from  $H_{AGN}$  (black points) and  $H_{noAGN}$  (white points) galaxies with  $V/\sigma < 1$  and a mass of  $\log(M_*/M_\odot) > 11$ . We also plot observational data from SLACS (red colors), SL2S (pink colors) and Newman et al. (2013) (green colors). Error bars indicate  $1\sigma$  standard deviations. AGN feedback seems to reproduce the observations well.

In view of all of these results, AGN feedback seems to be required to explain the observational trends.

### 3.3 Dependencies of $\gamma'_{tot}$ with $\gamma'_{dm}$ and $\gamma'_*$

In this section, we investigate the variations of  $\gamma'_{tot}$  with either the stellar slope  $\gamma'_*$  or the dark matter slope  $\gamma'_{dm}$  for galaxies with a mass greater than  $10^{11} M_\odot$  and  $V/\sigma < 1$  at  $z = 0.3$ . Results from HORIZON-AGN and HORIZON-NOAGN simulations are presented in Fig. 5. First, when AGN feedback is included, one can notice that  $\gamma'_{tot}$  and  $\gamma'_{dm}$  are strongly correlated. Regarding the dependence of  $\gamma'_{tot}$  and  $\gamma'_*$ , the dispersion is higher and the correlation is less clear but the important point here is that AGN feedback tends to limit the total slope to values close to 2 for the less massive galaxies while it reduces  $\gamma'_{tot}$  in the more massive ones compared to the simulation without AGN, which is consistent with the observations. On the contrary, in the absence of AGN feedback, we found again the opposite trends:  $\gamma'_{tot}$  and  $\gamma'_*$  are this time strongly correlated and due to stronger adiabatic contraction,  $\gamma'_{dm}$  reach values too high in more massive objects (see Peirani et al. 2017).

Another way to look into those variations and potential strong correlations between the three different density slopes is to consider the two dimensional plots of Fig. 6 showing the variations of  $\gamma'_*$  and  $\gamma'_{dm}$  with a color code representing the values of  $\gamma'_{tot}$  for galaxies with a mass greater than  $10^{11} M_\odot$  and  $V/\sigma < 1$  at  $z = 0$ . Note that this time we use the matching algorithm to

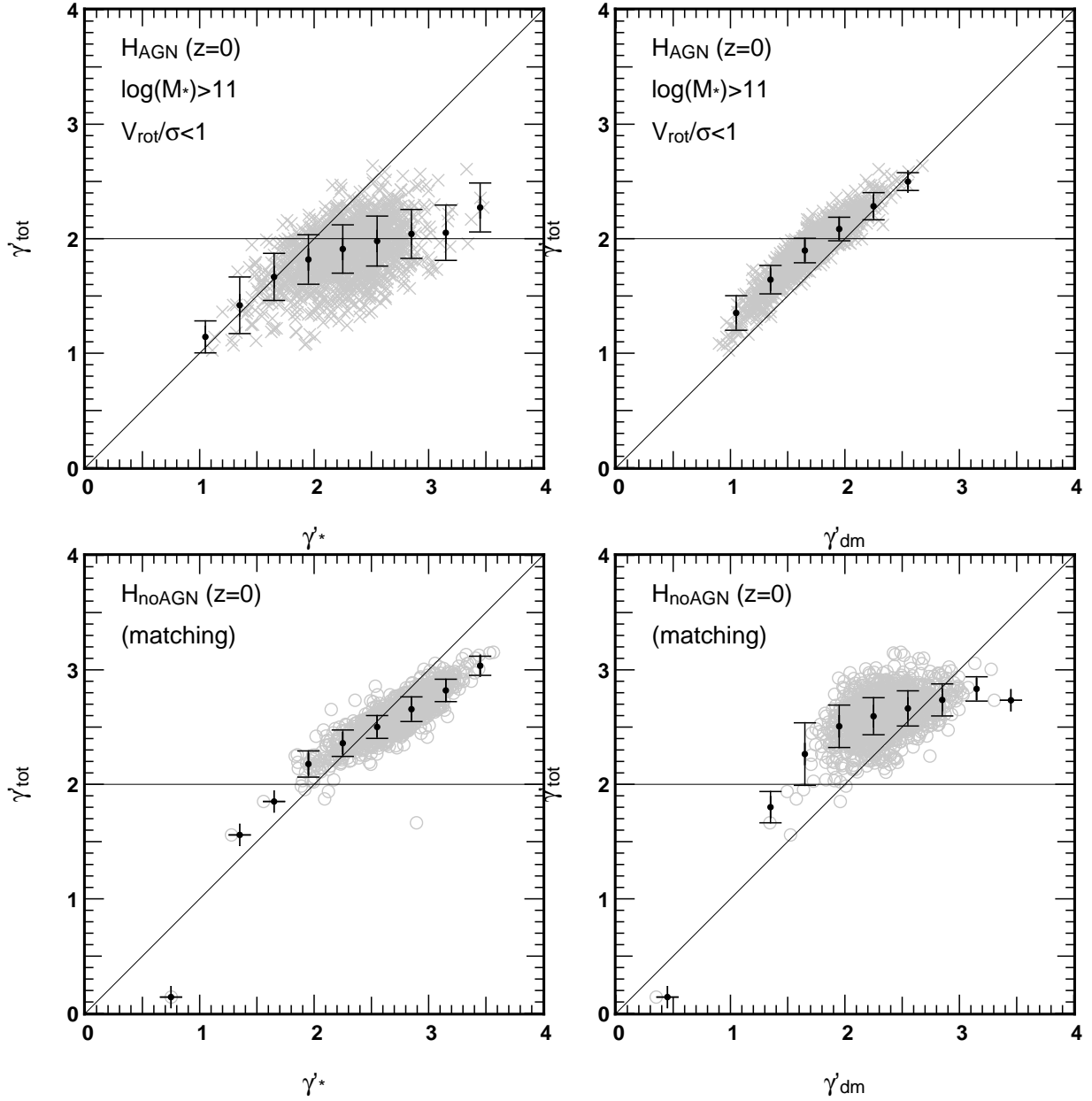


**Figure 5.** First line: the variations of the mass-weighted total density slope  $\gamma'_{\text{tot}}$  with respect to the mass-weighted stellar density slope  $\gamma'_*$  (first column) or the mass-weighted dark matter density slope  $\gamma'_{\text{dm}}$  (second column) for  $H_{\text{AGN}}$  galaxies with a mass greater than  $10^{11} M_{\odot}$  and  $V/\sigma < 1$  at  $z=0$ . Results from the matching  $H_{\text{noAGN}}$  galaxies are displayed in the second line. The horizontal solid line represents  $\gamma'_{\text{tot}} = 2$  generally obtained in the observation while the diagonal one is  $y = x$ .

select the  $H_{\text{noAGN}}$  galaxies which has the advantage, beside comparing the same objects between the simulations, to us to consider a higher number of  $H_{\text{noAGN}}$  galaxies. Indeed, most of the massive  $H_{\text{noAGN}}$  galaxies are disk-dominated and do not then satisfied  $V/\sigma < 1$  (see Dubois et al. 2016). However, we have checked that no significant differences are obtained if  $H_{\text{noAGN}}$  galaxies were selected using the same mass and  $V/\sigma$  criteria. Thus, the plots presented in Fig. 6 give the possible pairs  $(\gamma'_{\text{dm}}, \gamma'_*)$  for a given value of  $\gamma'_{\text{tot}}$ . We also see the linear correlations between  $\gamma'_{\text{tot}}$  and  $\gamma'_{\text{dm}}$  and between  $\gamma'_{\text{tot}}$  and  $\gamma'_*$  when AGN is included or not respectively.

The strong correlations seen between  $\gamma'_{\text{tot}}$  and  $\gamma'_{\text{dm}}$

or  $\gamma'_{\text{tot}}$  and  $\gamma'_*$  when AGN is included or not respectively can be easily understood when studying the density profile of the different components of a single object shown in Fig. 7. When AGN are included, galaxies are more extended and therefore have higher effective radii in general. Consequently, the dark matter is the dominant component at the effective radius scale. On the contrary, galaxies are found to be very compact in the absence of AGN activity and have therefore a smaller effective radius. In this case, the stellar component is the dominant component at the effective radius scale as is clearly shown in Fig. 7.

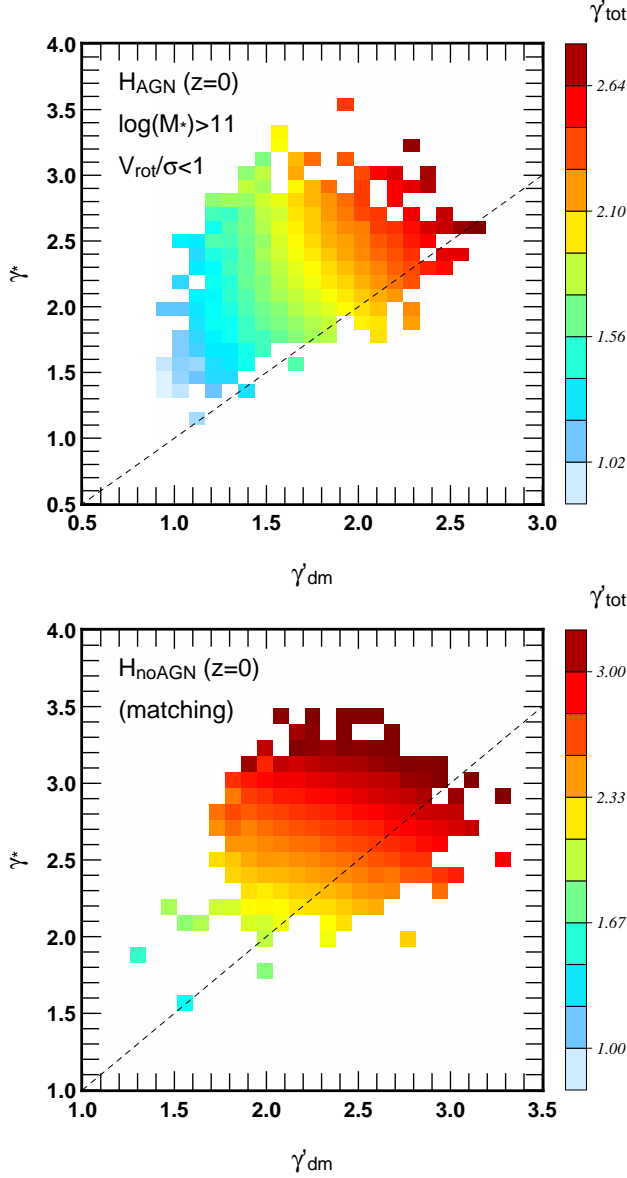


**Figure 6.** The variations of the mass-weighted stellar density slope  $\gamma'_*$  with respect to the mass-weighted dark matter density slope  $\gamma'_{dm}$  for  $H_{AGN}$  galaxies with a mass greater than  $10^{11} M_\odot$  and  $V/\sigma < 1$  at  $z=0$  (upper panel) and matching  $H_{noAGN}$  galaxies (lower panel). The color code represents values of the mass-weighted total density slope  $\gamma'_{tot}$ . The dashed line indicates  $y = x$ .

### 3.4 Evolution of $\gamma'_{tot}$ between $0 \leq z \leq 2$

One of the main objectives of this paper is to make theoretical predictions of the time evolution of  $\gamma'_{tot}$  of massive ETGs. Fig. 8 presents the time evolution of  $\gamma'_{dm}$ ,  $\gamma'_*$  and  $\gamma'_{tot}$  for  $H_{AGN}$  galaxies with a mass greater than  $10^{11} M_\odot$  and  $V/\sigma < 1$  in the redshift range  $0 \leq z \leq 2$ . We also impose  $R_e > 5$  kpc in order to be not too close to the lower resolution limit. We also derived the evolution for associated  $H_{noAGN}$  galaxies. Note that we analyse here the evolution from  $z = 2$  since our resolution does not enable us to properly estimate the differ-

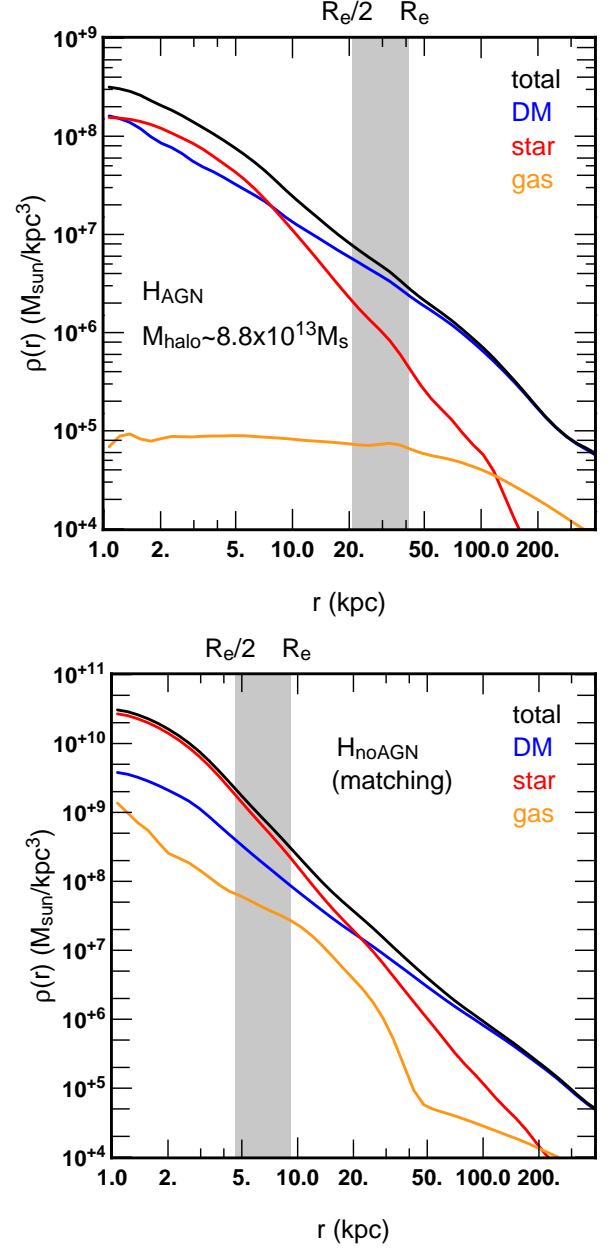


**Figure 7.** The total density profile (black lines) of the same massive dark matter halo extracted from the HORIZON-AGN (upper) and HORIZON-NOAGN (lower) simulations at  $z = 0$ . The dark matter, stellar and gas components are also shown in blue, red and orange colors respectively. The grey shade areas indicate the range of  $[R_e/2 - R_e]$  i.e. where we compute  $\gamma'_{tot}$ ,  $\gamma'_*$  and  $\gamma'_{dm}$ .

ent density slopes at higher  $z$  as typical effective radii of galaxies at higher redshift become too small. When considering  $H_{AGN}$  galaxies, we see a slight increase with time of the dark matter and total density slopes while the stellar density slope is nearly constant and close to 2.3 in the considered redshift interval. This means that the dark matter and total density profiles estimated at the effective radius tend to become slightly steeper at low redshifts while the stellar one does not vary signif-



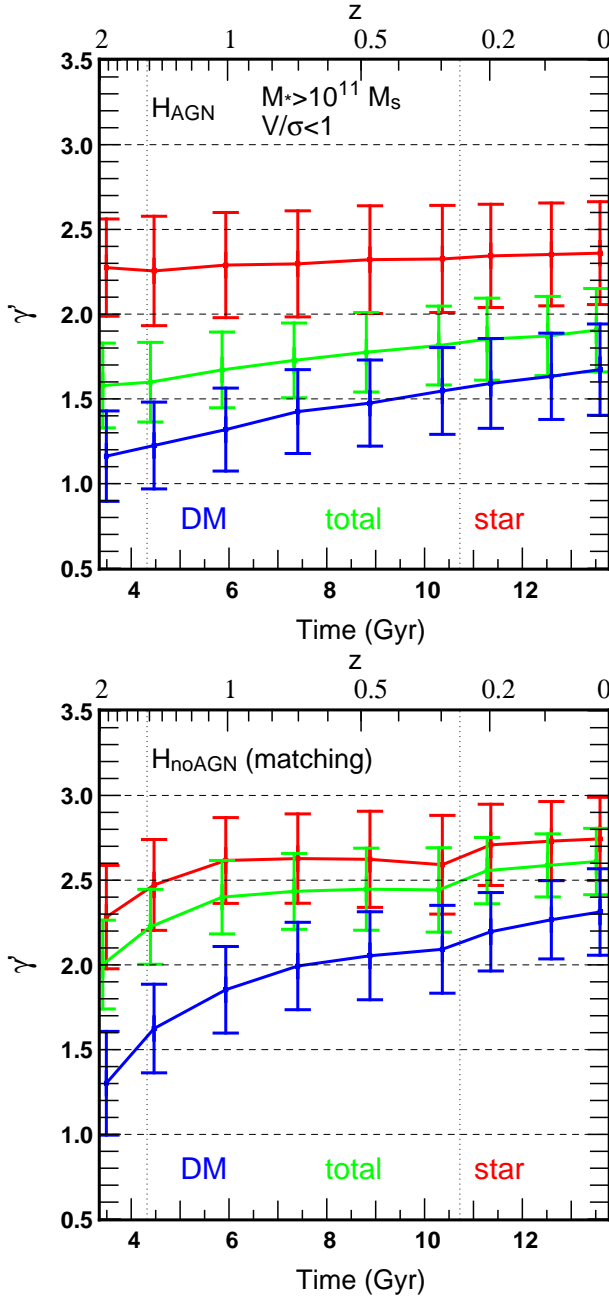


**Figure 8.** First line: the time evolutions of the mass-weighted total density slope  $\gamma'_{tot}$  (green lines) for  $H_{AGN}$  galaxies with  $V/\sigma < 1$ , a mass greater than  $10^{11} M_{\odot}$  and  $R_e > 5$  kpc. We also show the variations of the stellar ( $\gamma'_*$ ) and dark matter ( $\gamma'_{dm}$ ) components in red and blue lines respectively. The same evolutions obtained from the matching  $H_{noAGN}$  galaxies are displayed in the second line. Error bars are  $1\sigma$  standard deviations. The vertical dotted lines indicate the times when a new refinement level is added in the simulations.

icantly. The situation is slightly different for matching  $H_{noAGN}$  galaxies. In this case, contrary to  $\gamma'_{dm}$  which is increasing,  $\gamma'_*$  and therefore  $\gamma'_{tot}$  seem to be almost constant after  $z = 1$ . Note that an additional level of refinement occurs at  $z \sim 0.25$ . The extra star formation spuriously induced at this epoch increases the central

stellar mass, and induces a bump in the evolutions of  $\gamma'_*$ ,  $\gamma'_{dm}$  (by adiabatic contraction) and therefore  $\gamma'_{tot}$ . But despite this, it appears clearly that when AGN is not taken into account, the density slopes of each component is always higher than  $H_{AGN}$  counterparts.

Finally, we directly compare the evolution of  $\gamma'_{tot}$  to observations in Fig. 9. We consider here again galaxies satisfying  $M_* \geq 10^{11} M_{\odot}$ ,  $V/\sigma < 1$  and  $R_e > 5$  kpc in the redshift range of  $0 \leq z \leq 2$ . In the absence of AGN feedback, the derived  $\gamma'_{tot}$  values are too high compared to observations, as expected. When AGN feedback is included, the derived  $\gamma'_{tot}$  values are this time slightly too low. The observational data suggest that  $\gamma'_{tot}$  is also slightly increasing in the interval  $0 \leq z \leq 0.8$  though there is a large dispersion in the data. Our theoretical prediction from HORIZON-AGN exhibits much better agreement but it is not yet fully satisfactory. The discrepancies with observations could be explained by the fact that the  $H_{AGN}$  galaxies are too extended as shown in Fig. 1. Having galaxies slightly more compact, especially for the low mass ellipticals, will tend to increase values of  $\gamma'_{tot}$  and therefore improve greatly matching with observations.

For a more accurate comparison between our predictions and observations, we need to take into account the additional dependence of  $\gamma'_{tot}$  on stellar mass and size. In other words, at each  $z$ , we need to compare the average  $\gamma'_{tot}$  of our simulated galaxies with the average  $\gamma'_{tot}$  observed for galaxies with the same values of  $M_*$  and  $R_e$ . The latter can be obtained by evaluating Equation (2) at the same  $M_*$  and  $R_e$  as the simulation average. This gives us a band which is in general different from the simple average over data points. In Fig 9, we plot the curves relative to the 16, 50 and 84 percentile of the distribution (green lines). One can notice that, after removing the dependence on mass and size,  $\langle \gamma'_{tot} \rangle$  is still increasing and therefore this increase should not be due to the size-redshift evolution of ETGs galaxies.

The slight increase of  $\gamma'_{tot}$  in the considered redshift interval seems to be due to the increase of the density slope of the DM component as suggested by Figs 5, 6 and 8. As shown in Peirani et al. (2017), the evolution of the inner part of HORIZON-AGN haloes exhibit a condensation phase or “cusp regeneration” from  $z \sim 1.6$  down to  $z = 0$ . This phase is associated with a decrease of the evolution of the mass accretion on to black holes (BHs)  $\dot{M}_{BH} \equiv dM_{BH}/dt$  and therefore the AGN activity (see Fig 5 in Peirani et al. (2017)). Indeed, as advocated by Peirani et al. (2008) and Martizzi et al. (2013), repetitive cycles of gas expansion by AGN feedback (preferably through quasar mode) and gas cooling can efficiently flatten the inner part of dark matter profiles. If the AGN activity progressively decreases, this proposed mechanism becomes less efficient at counterbalancing the DM adiabatic contraction and at keeping the DM density profiles flat. Note that the density slope of the DM component in the HORIZON-NOAGN run is also increasing due to the same physical effect namely the adiabatic contraction. However, this not really affect the evolution of the total density profile as this latter mainly depends on the evolution of the stellar component.

Sonnenfeld et al. (2013b) have shown that the dependence of  $\gamma'_{tot}$  on the structure of ETGs can be well summarized with a dependence on stellar mass density  $\Sigma_* = M_*/(2\pi R_e^2)$ , leaving little dependence on  $M_*$  and  $R_e$  individually. Equation (2) can then be simplified as follows:

$$\langle \gamma'_{tot} \rangle = \gamma'_0 + \alpha(z - 0.3) + \eta(\log \Sigma_* - 9). \quad (2)$$

Sonnenfeld et al. (2013b) measured a value of  $\eta = 0.38 \pm 0.07$  from the sample of SLACS and SL2S lenses. Our  $H_{AGN}$  model is able to reproduce the observed trend with  $\Sigma_*$ , as shown in Fig. 10. By fitting our distribution of  $\gamma'_{tot}$  as a function of  $\Sigma_*$  for galaxies at  $z = 0.3$ , we find  $\eta = 0.31 \pm 0.04$ , in good agreement with the Sonnenfeld et al. (2013b) value. But once again, since the  $H_{AGN}$  galaxies tend to be too extended, the derived  $\Sigma_*$  values are too small compared to the observational values from the same galaxy mass range. This raises an additional question: we have used Equation (2) to estimate the observed  $\gamma'_{tot}$  for galaxies with the same mass and size as the simulated ones, however there is little overlap in stellar mass density between the SLACS and SL2S lenses and the  $H_{AGN}$  galaxies. The use of Equation (2) for our simulation is then, strictly speaking, an extrapolation. Nevertheless, Newman et al. (2015) showed how a very similar correlation between  $\gamma'_{tot}$  and  $\Sigma_*$  holds down to  $\log \Sigma_* = 8.0$ . Our use of Equation (2) in the stellar mass density regime probed by the  $H_{AGN}$  galaxies is then supported by observations.

#### 4 DISCUSSION AND CONCLUSIONS

By comparing results from two state-of-the-art hydrodynamical cosmological simulations whose only difference is the presence/absence of AGN feedback, we have explored the impact of AGN feedback on the evolution of the total density profiles of massive early-type galaxies. We mainly focused on galaxies with a mass greater than  $10^{11} M_\odot$  and satisfying  $V/\sigma < 1$ . Our findings can be summarized as follows:

- In the absence of AGN feedback, the simulated galaxies are clearly too compact with an effective radius too small, compared to observational data. On the contrary, AGN feedback tends to form more extended galaxies as already noted by Dubois et al. (2013, 2016). In this case, high-mass ellipticals in HORIZON-AGN seem to be in good agreement with the observations while low-mass ellipticals are not compact enough.
- When studying the variations of  $\gamma'_{tot}$  with the effective radius, the galaxy mass and the host halo mass at  $z = 0.3$ , we found that the inclusion of AGN feedback is required to get satisfactory agreement with observational values and trends.
- $\gamma'_{tot}$  is strongly correlated with  $\gamma'_{dm}$  when AGN feedback is included. On the contrary,  $\gamma'_{tot}$  is strongly correlated with  $\gamma'_*$  in the absence of AGN feedback.
- $\gamma'_{tot}$  is slightly increasing between  $0 \leq z \leq 2$ . This is due to the fact that when AGN is included, the evolution of  $\gamma'_{tot}$  is correlated with the evolution of  $\gamma'_{dm}$ . In Peirani et al. (2017), we indeed found that the dark

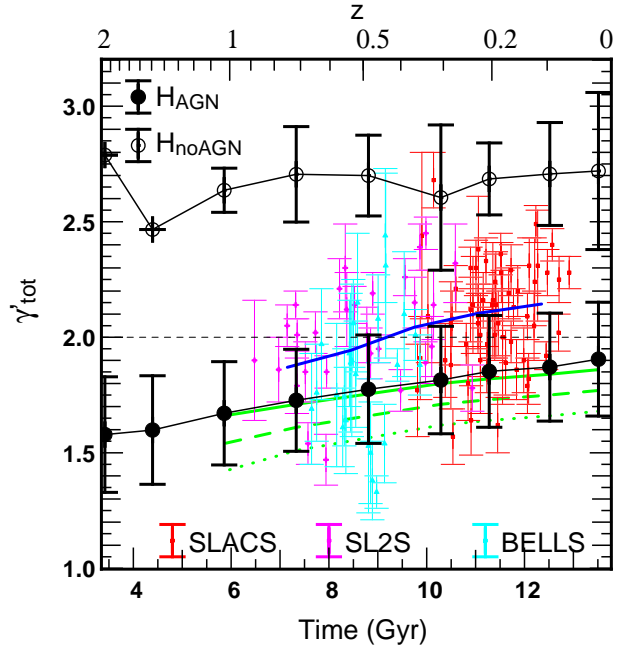


**Figure 9.** The time evolutions of the mass-weighted total density slope  $\gamma'_{tot}$  for  $H_{AGN}$  (black points) and  $H_{noAGN}$  (white points) galaxies satisfying  $V/\sigma < 1$ ,  $M_* \geq 10^{11} M_\odot$  and  $R_e > 5$  kpc in the considered redshift interval. We also add the observational data from the SLACS (red), SL2S (purple) and BELLS (cyan). The solid blue line shows the mean evolution derived from all observational data. The solid, dashed and dotted green lines are derived from respectively the 84, 50 and 16 percentiles of the probability distribution function of  $\langle \gamma'_{tot} \rangle$  from Equation (2). They represent the mean evolutions of  $\gamma'_{tot}$  after removing the dependence on stellar mass density (see details in the text). Error bars are  $1\sigma$  standard deviations.

matter density slope is increasing at low redshift because the AGN activity is reduced.

One interesting prediction of the present analysis is the evolution of  $\gamma'_{tot}$  over cosmic time. Because of our limited resolution (1 physical kpc), we could only consider the interval  $0 \leq z \leq 2$ . When AGN are included, we found that  $\gamma'_{tot}$  is slightly increasing with time. Compared to observational values, this trend is quite consistent, although the simulated values are slightly too low. This could be explained by the fact that the less massive  $H_{AGN}$  galaxies in our samples seem to be too extended. It is worth mentioning that observations from strong lensing by Ruff et al. (2011b) and Bolton et al. (2012) suggest that the total density profile of massive galaxies has become slightly steeper over cosmic time, in agreement with our findings. However, using well resolved hydrodynamical simulations, Remus et al. (2017); Xu et al. (2017) found the opposite trend i.e.,  $\gamma'_{tot}$  is decreasing after  $z = 2$ . Probably, the key point here is the behaviour and values of  $\gamma'_{tot}$  before  $z = 2$ . If important sources of feedback (e.g. AGN quasar mode) can flatten the dark matter and stellar components at high redshift (e.g. Peirani et al. 2008; Martizzi et al. 2013), then it would be difficult to sustain such flat profiles at lower redshift if feedback become less effi-

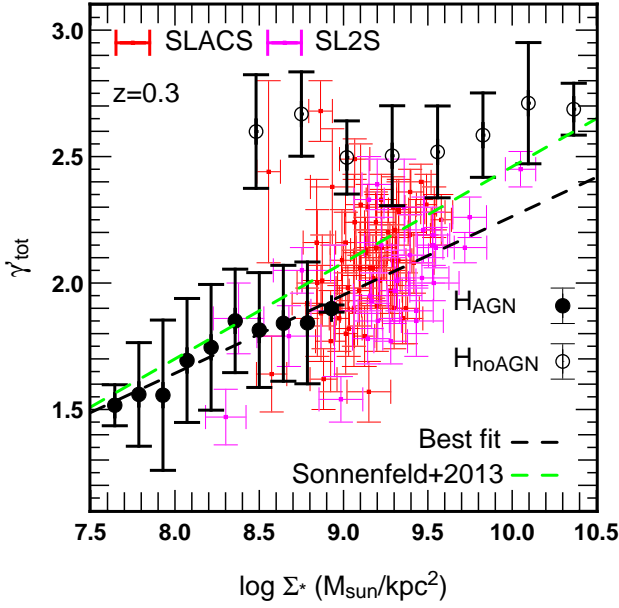


**Figure 10.** The variations of the mass-weighted total density slopes  $\gamma'_{tot}$  as a function of stellar mass density at  $z = 0.3$ . We consider here the same samples of simulated galaxies than previously. The black dashed line is the best fit measuring the inference on the parameter describing the dependence on  $\Sigma_*$  namely  $\eta = 0.31 \pm 0.04$ . The green dashed one indicates  $\eta = 0.38 \pm 0.07$  derived from observations (see Sonnenfeld et al. 2013b).

cient as advocated by Peirani et al. (2017). On the contrary, if these different components are already steep at  $z = 2$ , then mechanisms such as (dry) major mergers (Sonnenfeld et al. 2014) or efficient feedback could more easily flatten them at low redshift. The observational data of the SLACS, SL2S and BELLS seems to suggest that  $\gamma'_{tot}$  is slightly increasing but future detailed observational data, especially before  $z = 2$ , will definitely help to constrain the different scenarios and theoretical models.

### Acknowledgements

We are grateful to the referee Alan R. Duffy and the editor Joop Schaye for giving constructive comments which substantially helped improving the quality of the paper. We warmly thank M. Schaller for providing relevant Eagle simulation data. S.P. acknowledges support from the Japan Society for the Promotion of Science (JSPS long-term invitation fellowship). This work was granted access to the HPC resources of CINES under the allocations 2013047012, 2014047012 and 2015047012 made by GENCI and has made use of the Horizon cluster hosted by the Institut d’Astrophysique de Paris on which the simulation was post-processed. This work is supported in part by JSPS KAKENHI Grant Number JP26800093, JP15H05892 and JP17K14250 and by World Premier International Research Center Initiative (WPI Initiative), MEXT, Japan. The research of J.D. is supported by Adrian Beecroft and STFC. The research of J.S. has been sup-

ported at IAP by ERC project 267117 (DARK) hosted by Université Pierre et Marie Curie - Paris 6. This work was carried out within the framework of the Horizon project (<http://www.projet-horizon.fr>) and is partially supported by the grants ANR-13-BS05-0005 of the French Agence Nationale de la Recherche.

### REFERENCES

- Aubert, D., Pichon, C., & Colombi, S. 2004, MNRAS, 352, 376
- Auger, M. W., Treu, T., Bolton, A. S., et al. 2009, ApJ, 705, 1099
- Auger, M. W., Treu, T., Bolton, A. S., et al. 2010, ApJ, 724, 511
- Barnabè, M., Czoske, O., Koopmans, L. V. E., Treu, T., & Bolton, A. S. 2011, MNRAS, 415, 2215
- Beckmann, R. S., Devriendt, J., Slyz, A., et al. 2017, MNRAS, 472, 949
- Birnboim, Y. & Dekel, A. 2003, MNRAS, 345, 349
- Bolton, A. S., Brownstein, J. R., Kochanek, C. S., et al. 2012, ApJ, 757, 82
- Bolton, A. S., Burles, S., Koopmans, L. V. E., et al. 2008, ApJ, 682, 964
- Bolton, A. S., Burles, S., Koopmans, L. V. E., Treu, T., & Moustakas, L. A. 2006, ApJ, 638, 703
- Booth, C. M. & Schaye, J. 2009, MNRAS, 398, 53
- Brownstein, J. R., Bolton, A. S., Schlegel, D. J., et al. 2012, ApJ, 744, 41
- Cappellari, M. 2016, ARA&A, 54, 597
- Czoske, O., Barnabè, M., Koopmans, L. V. E., Treu, T., & Bolton, A. S. 2012, MNRAS, 419, 656
- Dekel, A., Birnboim, Y., Engel, G., et al. 2009, Nature, 457, 451
- Djorgovski, S. & Davis, M. 1987, ApJ, 313, 59
- Dressler, A., Lynden-Bell, D., Burstein, D., et al. 1987, ApJ, 313, 42
- Dubois, Y., Devriendt, J., Slyz, A., & Teyssier, R. 2010, MNRAS, 409, 985
- Dubois, Y., Devriendt, J., Slyz, A., & Teyssier, R. 2012, MNRAS, 420, 2662
- Dubois, Y., Gavazzi, R., Peirani, S., & Silk, J. 2013, MNRAS, 433, 3297
- Dubois, Y., Peirani, S., Pichon, C., et al. 2016, MNRAS, 463, 3948
- Dubois, Y., Pichon, C., Welker, C., et al. 2014, MNRAS, 444, 1453
- Duffy, A. R., Schaye, J., Kay, S. T., et al. 2010, MNRAS, 405, 2161
- Dutton, A. A., Macciò, A. V., Mendel, J. T., & Simard, L. 2013, MNRAS
- Dutton, A. A. & Treu, T. 2014, MNRAS, 438, 3594
- Dye, S., Negrello, M., Hopwood, R., et al. 2014, MNRAS, 440, 2013
- Faber, S. M., Dressler, A., Davies, R. L., Burstein, D., & Lynden-Bell, D. 1987, in Nearly Normal Galaxies. From the Planck Time to the Present, ed. S. M. Faber, 175–183
- Ferrarese, L. & Merritt, D. 2000, ApJ, 539, L9
- Gavazzi, R., Marshall, P. J., Treu, T., & Sonnenfeld, A. 2014, ApJ, 785, 144
- Gavazzi, R., Treu, T., Marshall, P. J., Brault, F., & Ruff, A. 2012, ApJ, 761, 170
- Gavazzi, R., Treu, T., Rhodes, J. D., et al. 2007, ApJ, 667, 176
- Gültekin, K., Richstone, D. O., Gebhardt, K., et al. 2009, ApJ, 698, 198

- Häring, N. & Rix, H.-W. 2004, *ApJ*, 604, L89
- Hirschmann, M., Naab, T., Somerville, R. S., Burkert, A., & Oser, L. 2012, *MNRAS*, 419, 3200
- Jiang, G. & Kochanek, C. S. 2007, *ApJ*, 671, 1568
- Jiménez-Vicente, J., Mediavilla, E., Kochanek, C. S., & Muñoz, J. A. 2015, *ApJ*, 799, 149
- Johansson, P. H., Naab, T., & Ostriker, J. P. 2012, *ApJ*, 754, 115
- Kaviraj, S., Laigle, C., Kimm, T., et al. 2017, *MNRAS*, 467, 4739
- Kereš, D., Katz, N., Weinberg, D. H., & Davé, R. 2005, *MNRAS*, 363, 2
- King, A. 2003, *ApJ*, 596, L27
- Komatsu, E., Smith, K. M., Dunkley, J., et al. 2011, *ApJS*, 192, 18
- Koopmans, L. V. E., Bolton, A., Treu, T., et al. 2009, *ApJ*, 703, L51
- Koopmans, L. V. E. & Treu, T. 2003, *ApJ*, 583, 606
- Koopmans, L. V. E., Treu, T., Bolton, A. S., Burles, S., & Moustakas, L. A. 2006, *ApJ*, 649, 599
- Lackner, C. N., Cen, R., Ostriker, J. P., & Joung, M. R. 2012, *MNRAS*, 425, 641
- Lackner, C. N. & Ostriker, J. P. 2010, *ApJ*, 712, 88
- Lagattuta, D. J., Fassnacht, C. D., Auger, M. W., et al. 2010, *ApJ*, 716, 1579
- Loeb, A. & Peebles, P. J. E. 2003, *ApJ*, 589, 29
- Magorrian, J., Tremaine, S., Richstone, D., et al. 1998, *AJ*, 115, 2285
- Martizzi, D., Teyssier, R., & Moore, B. 2013, *MNRAS*, 432, 1947
- Miralda-Escude, J. 1995, *ApJ*, 438, 514
- Natarajan, P. & Kneib, J.-P. 1996, *MNRAS*, 283, 1031
- Newman, A. B., Ellis, R. S., & Treu, T. 2015, *ApJ*, 814, 26
- Newman, A. B., Treu, T., Ellis, R. S., & Sand, D. J. 2013, *ApJ*, 765, 25
- Newman, A. B., Treu, T., Ellis, R. S., et al. 2009, *ApJ*, 706, 1078
- Nipoti, C., Treu, T., Auger, M. W., & Bolton, A. S. 2009, *ApJ*, 706, L86
- Nipoti, C., Treu, T., Leauthaud, A., et al. 2012, *MNRAS*, 422, 1714
- Ocvirk, P., Pichon, C., & Teyssier, R. 2008, *MNRAS*, 390, 1326
- Oguri, M., Rusu, C. E., & Falco, E. E. 2014, *MNRAS*, 439, 2494
- Omma, H., Binney, J., Bryan, G., & Slyz, A. 2004, *MNRAS*, 348, 1105
- Peirani, S., Dubois, Y., Volonteri, M., et al. 2017, *MNRAS*, 472, 2153
- Peirani, S., Kay, S., & Silk, J. 2008, *A&A*, 479, 123
- Posacki, S., Cappellari, M., Treu, T., Pellegrini, S., & Ciotti, L. 2015, *MNRAS*, 446, 493
- Power, C., Navarro, J. F., Jenkins, A., et al. 2003, *MNRAS*, 338, 14
- Rees, M. J. & Ostriker, J. P. 1977, *MNRAS*, 179, 541
- Remus, R.-S., Burkert, A., Dolag, K., et al. 2013, *ApJ*, 766, 71
- Remus, R.-S., Dolag, K., Naab, T., et al. 2017, *MNRAS*, 464, 3742
- Renzini, A. 2006, *ARA&A*, 44, 141
- Ruff, A. J., Gavazzi, R., Marshall, P. J., et al. 2011a, *ApJ*, 727, 96
- Ruff, A. J., Gavazzi, R., Marshall, P. J., et al. 2011b, *ApJ*, 727, 96
- Sand, D. J., Treu, T., & Ellis, R. S. 2002, *ApJ*, 574, L129
- Shaller, M., Frenk, C. S., Bower, R. G., et al. 2015, *MNRAS*, 452, 343
- Schaye, J., Crain, R. A., Bower, R. G., et al. 2015, *MNRAS*, 446, 521
- Schechter, P. L., Pooley, D., Blackburne, J. A., & Wambsganss, J. 2014, *ApJ*, 793, 96
- Shakura, N. I. & Sunyaev, R. A. 1973, *A&A*, 24, 337
- Shankar, F., Sonnenfeld, A., Mamon, G. A., et al. 2017, *ApJ*, 840, 34
- Sheth, R. K., Bernardi, M., Schechter, P. L., et al. 2003, *ApJ*, 594, 225
- Shu, Y., Bolton, A. S., Brownstein, J. R., et al. 2015, *ApJ*, 803, 71
- Shu, Y., Bolton, A. S., Mao, S., et al. 2016, *ApJ*, 833, 264
- Silk, J. & Rees, M. J. 1998, *A&A*, 331, L1
- Smith, R. J., Lucey, J. R., & Conroy, C. 2015, *MNRAS*, 449, 3441
- Sonnenfeld, A., Gavazzi, R., Suyu, S. H., Treu, T., & Marshall, P. J. 2013a, *ApJ*, 777, 97
- Sonnenfeld, A., Leauthaud, A., Auger, M. W., et al. 2018, *ArXiv e-prints*
- Sonnenfeld, A., Nipoti, C., & Treu, T. 2014, *ApJ*, 786, 89
- Sonnenfeld, A., Treu, T., Gavazzi, R., et al. 2013b, *ApJ*, 777, 98
- Sonnenfeld, A., Treu, T., Marshall, P. J., et al. 2015, *ApJ*, 800, 94
- Teyssier, R. 2002, *A&A*, 385, 337
- Tortora, C., La Barbera, F., Napolitano, N. R., et al. 2014, *MNRAS*, 445, 115
- Treu, T., Auger, M. W., Koopmans, L. V. E., et al. 2010, *ApJ*, 709, 1195
- Treu, T., Gavazzi, R., Gorecki, A., et al. 2009, *ApJ*, 690, 670
- Treu, T., Koopmans, L. V., Bolton, A. S., Burles, S., & Moustakas, L. A. 2006, *ApJ*, 640, 662
- Treu, T. & Koopmans, L. V. E. 2002, *ApJ*, 575, 87
- Treu, T. & Koopmans, L. V. E. 2004, *ApJ*, 611, 739
- Tu, H., Gavazzi, R., Limousin, M., et al. 2009, *A&A*, 501, 475
- van de Voort, F., Schaye, J., Booth, C. M., Haas, M. R., & Dalla Vecchia, C. 2011, *MNRAS*, 414, 2458
- Vogelsberger, M., Genel, S., Springel, V., et al. 2014, *MNRAS*, 444, 1518
- Volonteri, M., Dubois, Y., Pichon, C., & Devriendt, J. 2016, *MNRAS*, 460, 2979
- Welker, C., Dubois, Y., Devriendt, J., et al. 2017, *MNRAS*, 465, 1241
- White, S. D. M. & Frenk, C. S. 1991, *ApJ*, 379, 52
- White, S. D. M. & Rees, M. J. 1978, *MNRAS*, 183, 341
- Wyithe, J. S. B. & Loeb, A. 2003, *ApJ*, 595, 614
- Xu, D., Springel, V., Sluse, D., et al. 2017, *MNRAS*, 469, 1824

## APPENDIX A: RESOLUTION TESTS

In order to investigate the effects of resolution on our results, we compare our fiducial simulations (i.e. HORIZON-AGN) with lower resolution versions (i.e.  $512^3$  and  $256^3$  dark matter particles with initial uniform grid refined down to  $\Delta x = 2$  and  $\Delta x = 4$  proper kpc respectively). To have a clear diagnostic, we focus on the average density profiles of dark matter haloes at two epochs,  $z = 1$  and  $z = 0.3$ . In order to match dark matter haloes and galaxies between the three simulations, we use the same scheme developed in Peirani et al. (2017) and summarized in section 2.2. The main difference here is that one given dark matter particle of any of the two lower resolution simulations is associated to 8 parti-



cles in the subsequent higher resolution version (i.e. between HORIZON-AGN and HORIZON-AGN-512<sup>3</sup> or between HORIZON-AGN-512<sup>3</sup> and HORIZON-AGN-256<sup>3</sup>). However, it is still possible to know the composition of each dark matter halo and the fraction of common particles between two objects of different simulation versions. If this fraction is greater than 50%, we consider that these DM haloes are twin.

In the following, we select galaxy samples of a given mass range in the HORIZON-AGN simulation and at  $z = 1$  or  $z = 0.3$ . We then identified their matching galaxies in HORIZON-AGN-512<sup>3</sup> and HORIZON-AGN-256<sup>3</sup> when possible. Finally, we identify their respective host halo to produce samples of DM haloes between the three simulations. Only dark matter haloes which can be matched between the three simulations are kept.

Fig A1 compares the mean dark matter density profile for dark matter haloes hosting galaxies with a mass  $M_*$  defined by  $2 \times 10^{11} M_\odot \geq M_* \geq 10^{11} M_\odot$  at  $z = 1$ . In this case, we have considered 474 matched objects. As we can see, resolution effects cause the density to be overestimated in the inner parts of dark matter haloes. Moreover, as shown in Fig A2, we get the same trends at  $z = 0.3$  using a similar galaxy mass interval or considering more massive galaxies ( $M_* \geq 5 \times 10^{11} M_\odot$ ). We have considered here samples of 846 and 89 DM haloes respectively to derive the mean density profiles.

Power et al. (2003) recommend to use lower limit values of  $\sim 5$ , 10 and 20 kpc respectively for HORIZON-AGN, HORIZON-AGN (512<sup>3</sup>) and HORIZON-AGN (256<sup>3</sup>) and for our the studied halo/galaxy mass range. Although their analysis concerns pure dark matter simulations only, Figures A1 and A2 strongly suggest that lower limits defined by Power et al. (2003) give a clear and satisfactory indication of where the density profiles should converge.

Finally, we can also investigate the effect of resolution in the prediction of observable quantities relevant to this work such as the effective radius  $R_e$  and the total density slope  $\gamma'_{tot}$ . We therefore generate similar figures than Figs. 1, 2, 3 and 4 with adding results derived from HORIZON-AGN-512<sup>3</sup> and HORIZON-AGN-256<sup>3</sup>. One can see in Fig. A3 that the trends are quite similar between results from the three simulations, especially those relative to the variations of  $\gamma'_{tot}$  (upper right panel and lower ones). However, there are some slight differences induced by the baryon component treatment. Indeed, higher resolutions imply in general higher gas densities especially in the central part of haloes which can lead to more gas cooling. Therefore, the galaxies produced in the higher resolution simulations tend to be slightly more massive and more concentrated as the star formation tend to be more efficient in the inner regions. In this case, such galaxies have on the average lower  $R_e$  values as suggested by the upper left panel of Fig. A3. However, values of  $R_e$  from the considered stellar mass range are quite close between the different simulations and this seems not to particularly affect the estimation of  $\gamma'$  in the interval  $[R_e/2 - R_e]$ .

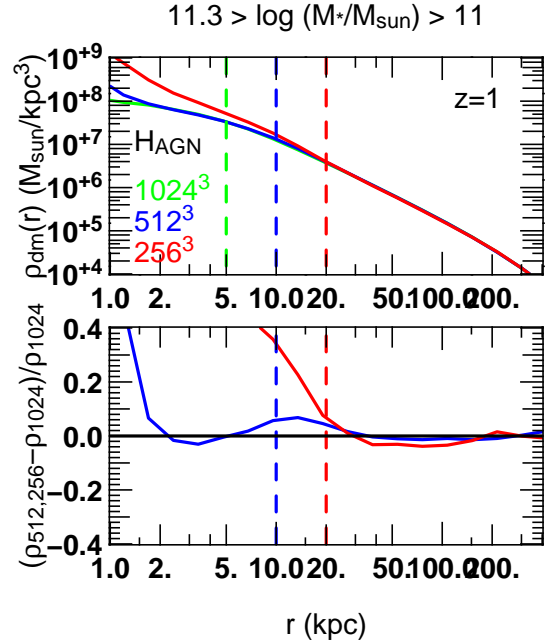


**Figure A1.** Comparison of the mean dark matter density profiles (and residual) of haloes hosting a galaxy with a mass of  $2 \times 10^{11} \geq M_* \geq 10^{11} M_\odot$  at  $z = 1$ , derived from the HORIZON-AGN simulation (green line) and lower resolution versions, HORIZON-AGN-512<sup>3</sup> (blue line) and HORIZON-AGN-256<sup>3</sup> (red line). The dashed vertical lines (with same color code) correspond to recommended lower limit values suggested by Power et al. (2003) for each simulation which give satisfactory indication of where the density profiles should converge.



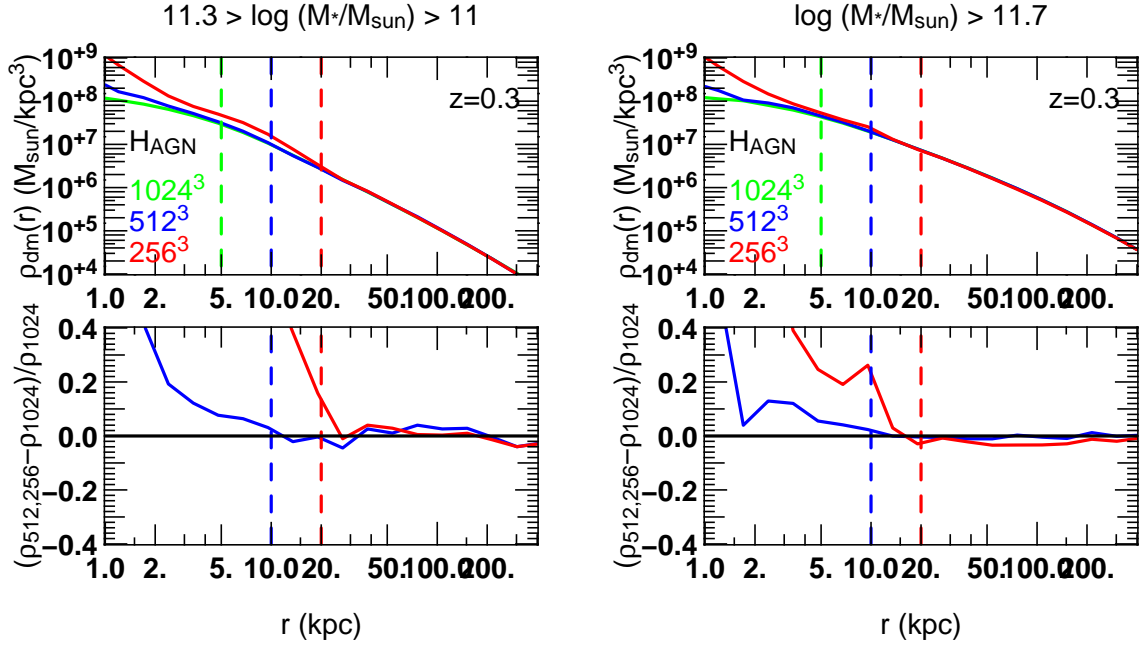


**Figure A2.** As in Fig. A1 but for DM haloes hosting a galaxy with a mass of  $2 \times 10^{11} M_{\odot} \geq M_* \geq 10^{11} M_{\odot}$  (left panel) or  $M_* \geq 5 \times 10^{11} M_{\odot}$  (right panel) at  $z = 0.3$ . Same trends are obtained.

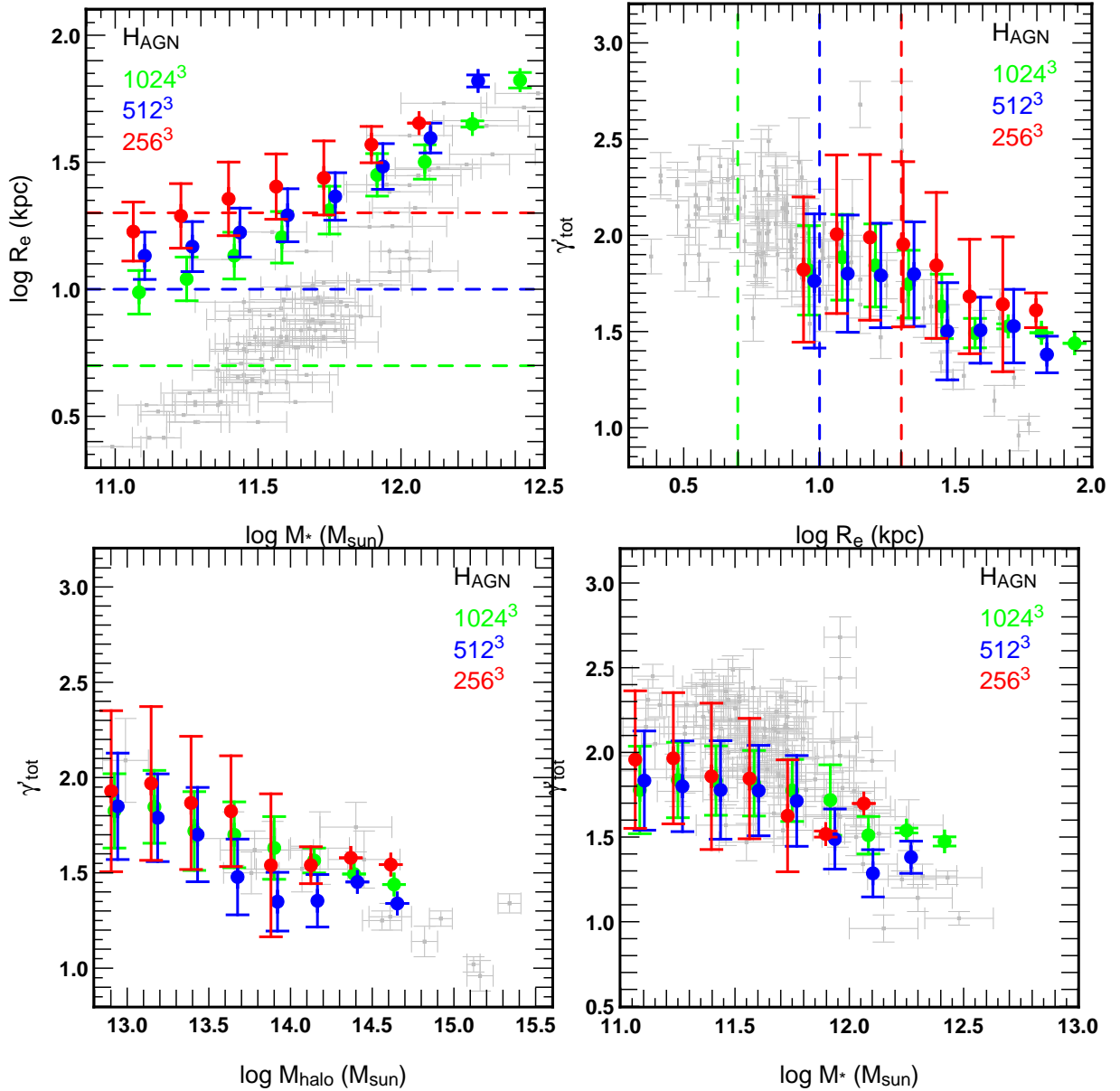


**Figure A3.** The variations of the effective radius  $R_e$  with respect to the stellar mass  $M_*$  (upper left panel) and the variations of the mass-weighted total density slopes  $\gamma'_{tot}$  with respect to the effective radius  $R_e$  (upper right panel), to the dark matter halo masses  $M_{halo}$  (lower left panel) and to the stellar masses  $M_*$  (lower right panel). Green color refers to our fiducial HORIZON-AGN simulation while blue et red colors correspond to results from matching galaxies from HORIZON-AGN-512<sup>3</sup> and HORIZON-AGN-256<sup>3</sup> respectively. The dashed lines (with same color code) correspond to recommended lower limit values suggested by Power et al. (2003) for each simulation. Grey data are observational data used in Fig. 1, 2, 3 and 4. In spite of slight differences, same trends are obtained from the three runs in the considered galaxy mass range.